CHAPTER

9

The Active Dendritic Tree

OUTLINE

We are now prepared to assemble models that are capable of reproducing the great variety of responses, seen in the laboratory, to synaptic input distributed in space and time. This requires only that we add ion channels to our passive dendrite. A combination of the numerical methods of Chapters 4 and 8 will permit us to generate the action potential launched by supra-threshold current injection and to study its propagation down the cell's axon and back up into the dendritic tree, in agreement with the recordings in Figure 9.1.

We then build a model for determining the extracellular current induced by such traveling action potentials and study its effect on neighboring cables like axons or dendrites. We next move on to synaptic initiation of somatic spikes and investigate the role of a specialized glutamate receptor, called the NMDA receptor, in acknowledging action potential back propagation into the dendrites. We next develop and study the quasi-active cable and demonstrate its ability to capture the cell's subthreshold response and resonant frequency. We then investigate synaptic attenuation and integration on our active fork prior to introducing and demonstrating MATLAB tools for the simulation of arbitrarily branched cells. Finally, we move on to the fully branched case, where we study synaptic integration.

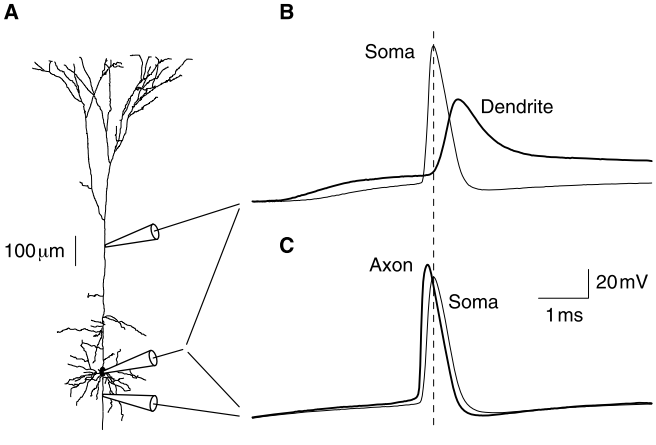

FIGURE 9.1 Action potential initiation and propagation in a pyramidal cell from layer 5 of the rat neocortex. **A**. Cell tracing and electrode locations in dendrite, soma and axon. **B**. Current injection at the soma generates a somatic action potential that propagates, with attenuation, back into the dendrites ≈ 270 μm in ≈ 1 ms. **C**. The somatic action potential also propagates, with amplification, down the axon ≈ 17 μm in ≈ 0.1 ms. From Stuart et al. (1997).

Mathematics for Neuroscientists, Second Edition
DOI: 10.1016/B978-0-12-801895-8.00009-9

9.1 THE ACTIVE UNIFORM CABLE

If we add the sodium and potassium currents of Chapter 4 to the passive cable of Chapter 6 we arrive at the active cable system

$$\begin{aligned} C_m \frac{\partial V}{\partial t} &= G_a \frac{\partial^2 V}{\partial x^2} - \overline{g}_{Na} m^3 h (V - V_{Na}) - \overline{g}_K n^4 (V - V_K) - g_{Cl}(V - V_{Cl}) + I_{stim}/(2\pi a) \\ \frac{\partial m}{\partial t} &= \alpha_m(V)(1-m) - \beta_m(V) m \\ \frac{\partial h}{\partial t} &= \alpha_h(V)(1-h) - \beta_h(V) h \\ \frac{\partial n}{\partial t} &= \alpha_n(V)(1-n) - \beta_n(V) n \end{aligned} \tag{9.1}$$

where $G_a = a/(2R_a)$ is the axial conductance. We assume that the cable is sealed

$$\frac{\partial V}{\partial x}(0,t) = \frac{\partial V}{\partial x}(\ell, t) = 0,$$

and that it begins at rest

$$V(x,0) = V_r,\ m(x,0) = m_\infty(V_r),\ h(x,0) = h_\infty(V_r),\ n(x,0) = n_\infty(V_r).$$

If the ionic conductances are uniformly distributed, i.e., their conductance densities do not vary with position, then the rest potential is in fact the same V_r as that in Eq. (4.16).

As Eq. (9.1) does not yield to elementary mathematical analysis we pursue its approximate solution. In particular, we choose a space-step, dx, and so study a cable with $N_x = \ell/dx$ compartments, and then choose a time-step, dt, and final time T and so march through $N_t = T/dt$ units of time. We evaluate our stimulus and approximate the response on the associated space–time grid

$$\begin{aligned} \mathtt{V}_i^j &\approx V((i-1/2)dx, (j-1)dt) \\ \mathtt{m}_i^j &\approx m((i-1/2)dx, (j-3/2)dt) \\ \mathtt{I}_i^j &= I_{stim}((i-1/2)dx, (j-3/2)dt)/(2\pi a), \quad i = 1, \ldots, N_x,\ j = 1, \ldots, N_t \end{aligned} \tag{9.2}$$

where $(i-1/2)dx$ is the midpoint of the ith compartment, as in Eq. (6.54), and the staggering of voltage and gating time grids conforms to our original choice, Eq. (4.17).

Arguing precisely as in Chapter 4 we may advance the gating variables via

$$\mathtt{m}_i^j = \frac{(1/dt - (\alpha_m(\mathtt{v}_i^{j-1}) + \beta_m(\mathtt{v}_i^{j-1}))/2)\mathtt{m}_i^{j-1} + \alpha_m(\mathtt{v}_i^{j-1})}{1/dt + (\alpha_m(\mathtt{v}_i^{j-1}) + \beta_m(\mathtt{v}_i^{j-1}))/2} \quad i = 1, \ldots, N_x. \tag{9.3}$$

We now collect the compartmental terms into columns

$$\mathtt{V}^j = (\mathtt{V}_1^j\ \mathtt{V}_2^j\ \cdots\ \mathtt{V}_{N_x}^j)^T, \quad \mathtt{m}^j = (\mathtt{m}_1^j\ \mathtt{m}_2^j\ \cdots\ \mathtt{m}_{N_x}^j)^T, \quad \text{etc.},$$

and advance $\mathtt{V}^{j-1}$ voltage by the half-step Backward Euler rule (per Eq. (4.20))

$$C_m \frac{\mathtt{V}^{j-1/2} - \mathtt{V}^{j-1}}{dt/2} = G_a \mathbf{S} \mathtt{V}^{j-1/2} - \overline{g}_{Na}(\mathtt{m}^j)^3 \mathtt{h}^j (\mathtt{V}^{j-1/2} - V_{Na}) - \overline{g}_K (\mathtt{n}^j)^4 (\mathtt{V}^{j-1/2} - V_K) - g_{Cl}(\mathtt{V}^{j-1/2} - V_{Cl}) + \mathtt{I}^j$$

where $\mathbf{S}$ is our standard second difference matrix, Eq. (6.9). We write this as a linear system for $\mathtt{V}^{j-1/2}$,

$$(\mathrm{diag}(\mathtt{d}^j + 2C_m/dt) + G_a \mathbf{S})\mathtt{V}^{j-1/2} = (2C_m/dt)\mathtt{V}^{j-1} + \mathtt{f}^j \tag{9.4}$$

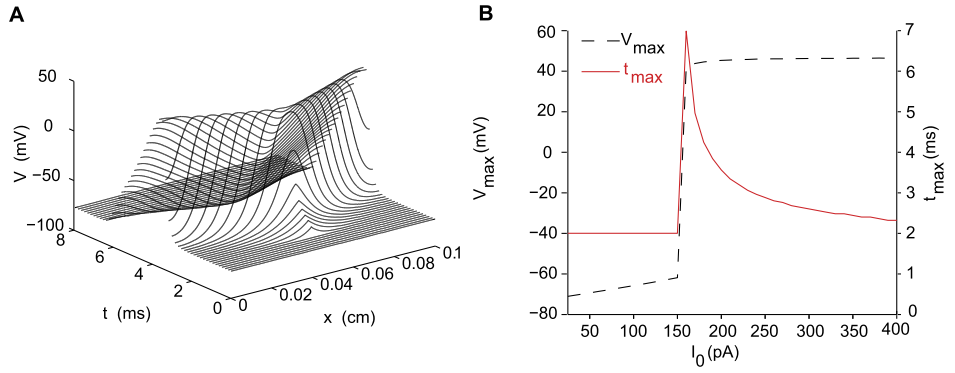

FIGURE 9.2 Response of the active cable described by Eqs. (6.17), (4.8)–(4.9) and (4.13)–(4.14) to a current pulse described by Eq. (9.6) with $x_s = 0.05$ cm. **A**. Full space–time response to supra-threshold input, $I_0 = 400$ pA. This stimulus has initiated an action potential that propagates at constant velocity in each direction. **B**. A plot of the maximum depolarization at x_s, and the time at which it occurred, as a function of stimulus amplitude, I_0. (`stEcab.m`)

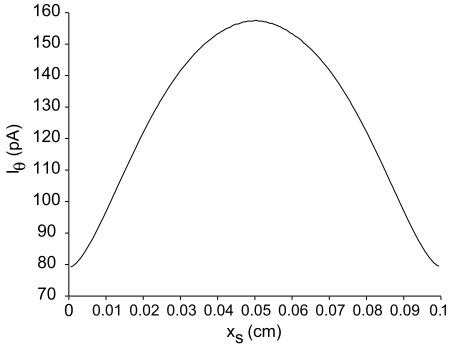

FIGURE 9.3 A plot of stimulus threshold, I_θ, as a function of stimulus location, x_s, for the cable described by Eqs. (6.17), (4.8)–(4.9) and (4.13)–(4.14) and a current pulse of the form Eq. (9.6). (`stEcabthreshloc.m`)

where the elements of `d` and `f` are

$$\mathtt{d}_i^j = \overline{g}_{Na}(\mathtt{m}_i^j)^3\mathtt{h}_i^j + \overline{g}_K(\mathtt{n}_i^j)^4 + g_{Cl} \quad \text{and} \quad \mathtt{f}_i^j = \overline{g}_{Na}(\mathtt{m}_i^j)^3\mathtt{h}_i^j V_{Na} + \overline{g}_K(\mathtt{n}_i^j)^4 V_K + g_{Cl}V_{Cl} + \mathtt{I}_i^j$$

respectively. We conclude, as in Eq. (4.21), with the final additional half-step update

$$\mathtt{V}^j = 2\mathtt{V}^{j-1/2} - \mathtt{V}^{j-1}. \tag{9.5}$$

We have coded this and illustrated its use in Figure 9.2 on the cable with size and passive parameters as in Eq. (6.17), active parameters and functionals as detailed in §§4.1 and 4.2, and a 1 ms stimulus

$$I_{stim}(x,t) = I_0 \mathbb{1}_{(1,2)}(t)\delta(x - x_s) \tag{9.6}$$

of amplitude I_0 delivered at $x = x_s$.

We see that a 1 ms current pulse at mid-cable ignites an action potential when I_0 exceeds the threshold, I_θ, of approximately 150 pA and we note that the V_{max}/I_0 curve differs very little from the isopotential case, Figure 4.7B. In the case of a cable, however, stimulus location can also play a major role. For current delivered near a sealed end sees a greater resistance and hence yields a greater depolarization. We make this precise in Figure 9.3.

The speed of the action potential wave illustrated in Figure 9.2A depends on both the geometry of the cable and the mix of currents crossing its lateral surface. We will investigate these dependencies in the exercises.

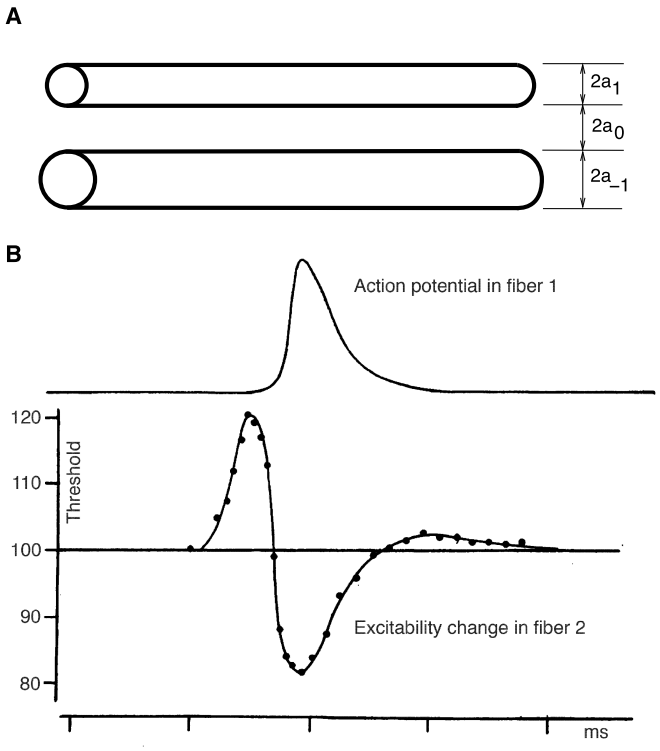

FIGURE 9.4 **A**. A schematic of two parallel cables. **B**. The electrical stimulation of fiber 1 and its effect on the threshold of fiber 2. Action potentials in fibers 1 and 2 are elicited by short electric pulses. An illustration of an action potential recorded from fiber 1 is on top. The threshold change is expressed as a percentage of the baseline value (100) observed in fiber 2 without stimulation of fiber 1 and is measured as a function of the stimulation interval between fiber 1 and 2. Initially the threshold is raised by the traveling action potential in fiber 1, but then the second fiber becomes more excitable followed by a period of slightly reduced excitability. In vitro preparation of a limb nerve of the crab. From Katz and Schmitt (1940).

9.2 ON THE INTERACTION OF ACTIVE UNIFORM CABLES*

There is ample evidence, see Figure 9.4, to support the investigation of the non-synaptic influence that an action potential traveling down a cable may have on its neighbors. These interactions are often deemed "ephaptic" and arise, for example, from extracellular currents and excess extracellular potassium associated with traveling action potentials.

In Exercise 4.5 we demonstrated that increased extracellular potassium depolarizes nearby cells. We here build and analyze a model, see Figure 9.5, of two parallel cables of radii a_1 and a_{-1}, separated by a distance $2a_0$, in which extracellular current may flow.

If the radii of the upper and lower cables are $a_{\pm 1}$ and dx is the length of a compartment then current balance at the nodes marked $\phi_{2,1}$ and $\phi_{2,-1}$ yields

$$2\pi a_1 dx\{C_m(\phi_{2,1}-\phi_{2,0})' + I_{ion}(\phi_{2,1}-\phi_{2,0})\} = \frac{\pi a_1^2}{R_a dx}(\phi_{1,1}-2\phi_{2,1}+\phi_{3,1})$$

$$2\pi a_{-1} dx\{C_m(\phi_{2,-1}-\phi_{2,0})' + I_{ion}(\phi_{2,-1}-\phi_{2,0})\} = \frac{\pi a_{-1}^2}{R_a dx}(\phi_{1,-1}-2\phi_{2,-1}+\phi_{3,-1}).$$

Next, as the fibers are separated by a distance of $2a_0$, current balance at the node marked $\phi_{2,0}$ yields

$$2\pi a_1 dx\{C_m(\phi_{2,1}-\phi_{2,0})' + I_{ion}(\phi_{2,1}-\phi_{2,0})\} + 2\pi a_{-1} dx\{C_m(\phi_{2,0}-\phi_{2,-1})' + I_{ion}(\phi_{2,0}-\phi_{2,-1})\} = -\frac{\pi a_0^2}{R_e dx}(\phi_{1,0}-2\phi_{2,0}+\phi_{3,0}).$$

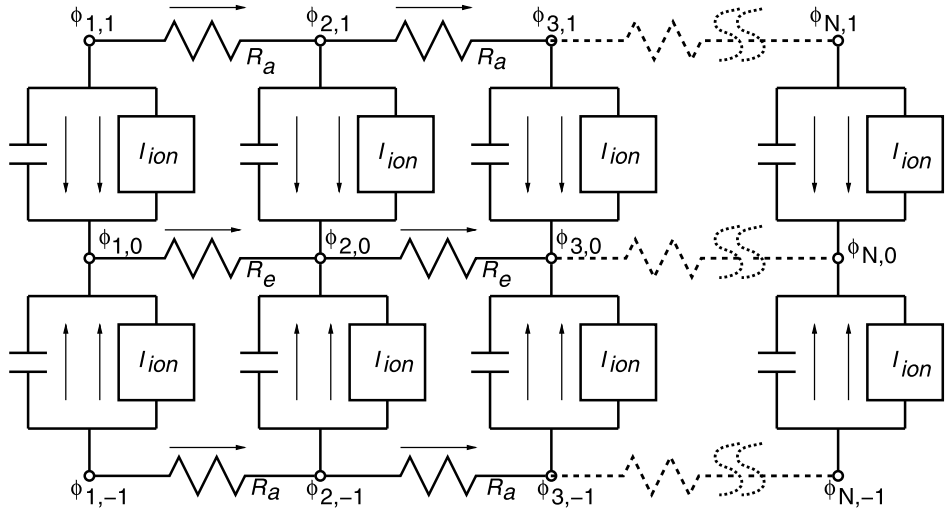

FIGURE 9.5 A circuit diagram, corresponding to Figure 9.4A, of two cables and the extracellular fluid that separates them. Here R_e is the effective axial resistance of the extracellular fluid, $\phi_{j,\pm1}$ denote the intracellular potentials of the respective cables, $\phi_{0,\pm1}$ denote the associated extracellular potentials, and the membrane currents, at each compartment, have been lumped into the I_{ion} boxes.

If we now define the transmembrane potentials

$$V_n \equiv \phi_{n,1} - \phi_{n,0} \quad \text{and} \quad W_n \equiv \phi_{n,-1} - \phi_{n,0}$$

the above become

$$C_m V_2' + I_{ion}(V_2) = \frac{a_1}{2R_a}\frac{V_1 - 2V_2 + V_3}{dx^2} + \frac{a_1}{2R_a}\frac{\phi_{1,0} - 2\phi_{2,0} + \phi_{3,0}}{dx^2}$$
$$C_m W_2' + I_{ion}(W_2) = \frac{a_{-1}}{2R_a}\frac{W_1 - 2W_2 + W_3}{dx^2} + \frac{a_{-1}}{2R_a}\frac{\phi_{1,0} - 2\phi_{2,0} + \phi_{3,0}}{dx^2}$$

and

$$a_1\{C_m V_2' + I_{ion}(V_2)\} + a_{-1}\{C_m W_2' + I_{ion}(W_2)\} = -\frac{a_0^2}{2R_e}\frac{\phi_{1,0} - 2\phi_{2,0} + \phi_{3,0}}{dx^2}.$$

On substituting the latter into the former we have

$$\frac{a_0^2 R_a + a_1^2 R_e}{a_0^2 R_a}\{C_m V_2' + I_{ion}(V_2)\} + \frac{a_1 a_{-1} R_e}{a_0^2 R_a}\{C_m W_2' + I_{ion}(W_2)\} = \frac{a_1}{2R_a}\frac{V_1 - 2V_2 + V_3}{dx^2} \tag{9.7}$$
$$\frac{a_0^2 R_a + a_{-1}^2 R_e}{a_0^2 R_a}\{C_m W_2' + I_{ion}(W_2)\} + \frac{a_{-1} a_1 R_e}{a_0^2 R_a}\{C_m V_2' + I_{ion}(V_2)\} = \frac{a_{-1}}{2R_a}\frac{W_1 - 2W_2 + W_3}{dx^2}. \tag{9.8}$$

Now $(a_0^2 R_a + a_{-1}^2 R_e)/(a_1 a_{-1} R_e)$ times Eq. (9.7) minus Eq. (9.8) brings

$$C_m V_2' + I_{ion}(V_2) = c_1 \frac{a_1}{2R_a}\frac{V_1 - 2V_2 + V_3}{dx^2} - c_2 \frac{a_{-1}}{2R_a}\frac{W_1 - 2W_2 + W_3}{dx^2}, \tag{9.9}$$

where the coupling parameters are

$$c_1 = \frac{a_0^2 R_a + a_{-1}^2 R_e}{a_0^2 R_a + (a_1^2 + a_{-1}^2) R_e} \quad \text{and} \quad c_2 = \frac{a_1 a_{-1} R_e}{a_0^2 R_a + (a_1^2 + a_{-1}^2) R_e}. \tag{9.10}$$

Similarly, $(a_0^2R_a + a_1^2R_e)/(a_1a_{-1}R_e)$ times Eq. (9.8) minus Eq. (9.7) brings

$$C_m W_2' + I_{ion}(W_2) = c_{-1}\frac{a_{-1}}{2R_a}\frac{W_1 - 2W_2 + W_3}{dx^2} - c_2\frac{a_1}{2R_a}\frac{V_1 - 2V_2 + V_3}{dx^2}, \tag{9.11}$$

where

$$c_{-1} = \frac{a_0^2R_a + a_1^2R_e}{a_0^2R_a + (a_1^2 + a_{-1}^2)R_e}.$$

Current balance at the remaining nodes proceeds exactly as above. As such we may express the full coupled system as

$$C_m\mathbf{u}'(t) + g_{Cl}(\mathbf{u}(t) - V_{Cl}) + \overline{g}_K\mathbf{n}^4(\mathbf{u} - V_K) + \overline{g}_{Na}^3\mathbf{h}(\mathbf{u} - V_{Na}) = \mathbf{B}\mathbf{u}(t) + \mathbf{f}(t), \tag{9.12}$$

where

$$\mathbf{u}(t) = \begin{pmatrix}\mathbf{v}(t)\\ \mathbf{w}(t)\end{pmatrix}$$

with $\mathbf{v}(t) = (V_1(t), \ldots, V_n(t))^T$ and $\mathbf{w}(t) = (W_1(t), \ldots, W_n(t))^T$. The matrix $\mathbf{B}$ is defined by

$$\mathbf{B} = \begin{pmatrix} c_1G_1\mathbf{S} & -c_2G_{-1}\mathbf{S}\\ -c_2G_1\mathbf{S} & c_{-1}G_{-1}\mathbf{S}\end{pmatrix},$$

with $G_{\pm1} = a_{\pm1}/(2R_a)$ and $\mathbf{S}$ is our familiar second difference matrix. The gating variables continue to obey equations of the form

$$\mathbf{m}'(t) = \frac{m_\infty(\mathbf{u}(t)) - \mathbf{m}(t)}{\tau_m(\mathbf{u}(t))}.$$

We recognize that the off-diagonal elements of $\mathbf{B}$ capture the interaction of the two cables. In particular, each cable "stimulates" the other through a current that is proportional to the spatial second difference of its membrane potential. In addition, as $c_{\pm1} < 1$, we note that the effective individual axial conductances, $c_{\pm1}G_{\pm1}$, are each smaller than their original values.

We may proceed, as in the case of a single cable, to apply the staggered Euler scheme to Eq. (9.12). We have implemented this in `stE2cab.m` and demonstrate its findings in Figure 9.6.

In reality both cables would be receiving independent input and rather than the first cable fully exciting the second, it is more likely that activity in the first serves to lower the second's threshold for excitation. This is the scenario illustrated in Figure 9.4 and we will investigate it further in the exercises.

It may perhaps be easier to visualize the interaction terms by passing to the limit, $dx \to 0$, in Eq. (9.12) and so arriving at the coupled active cable equations

$$\begin{aligned} C_m\frac{\partial V}{\partial t} + g_{Cl}(V - V_{Cl}) + \overline{g}_K n_1^4(V - V_K) + \overline{g}_{Na}m_1^3h_1(V - V_{Na}) &= c_1G_1\frac{\partial^2 V}{\partial x^2} - c_2G_{-1}\frac{\partial^2 W}{\partial x^2} + I_{stim}/(2\pi a_1)\\ C_m\frac{\partial W}{\partial t} + g_{Cl}(W - V_{Cl}) + \overline{g}_K n_2^4(W - V_K) + \overline{g}_{Na}m_2^3h_2(W - V_{Na}) &= c_{-1}G_{-1}\frac{\partial^2 W}{\partial x^2} - c_2G_1\frac{\partial^2 V}{\partial x^2}\end{aligned}$$

where

$$\frac{\partial m_1}{\partial t} = \frac{m_\infty(V) - m_1}{\tau_m(V)} \quad \text{and} \quad \frac{\partial m_2}{\partial t} = \frac{m_\infty(W) - m_2}{\tau_m(W)},$$

and similarly for the remaining gating equations. The two potential equations now make it clear that it is the axial current in a cable that stimulates its neighboring cables. In particular, with regard to Figure 9.6E, we see that as the top cable fires, its membrane potential, V, at fixed time t, progresses from a single concave bump to two concave bumps traveling away from the site of initiation. Where V is concave we know that $\partial^2 V/\partial x^2 \leq 0$ and so the stimulus to the lower cable is positive. Hence, as the V wave travels in the upper cable it reinforces, and is likewise reinforced by, the W wave in the lower cable.

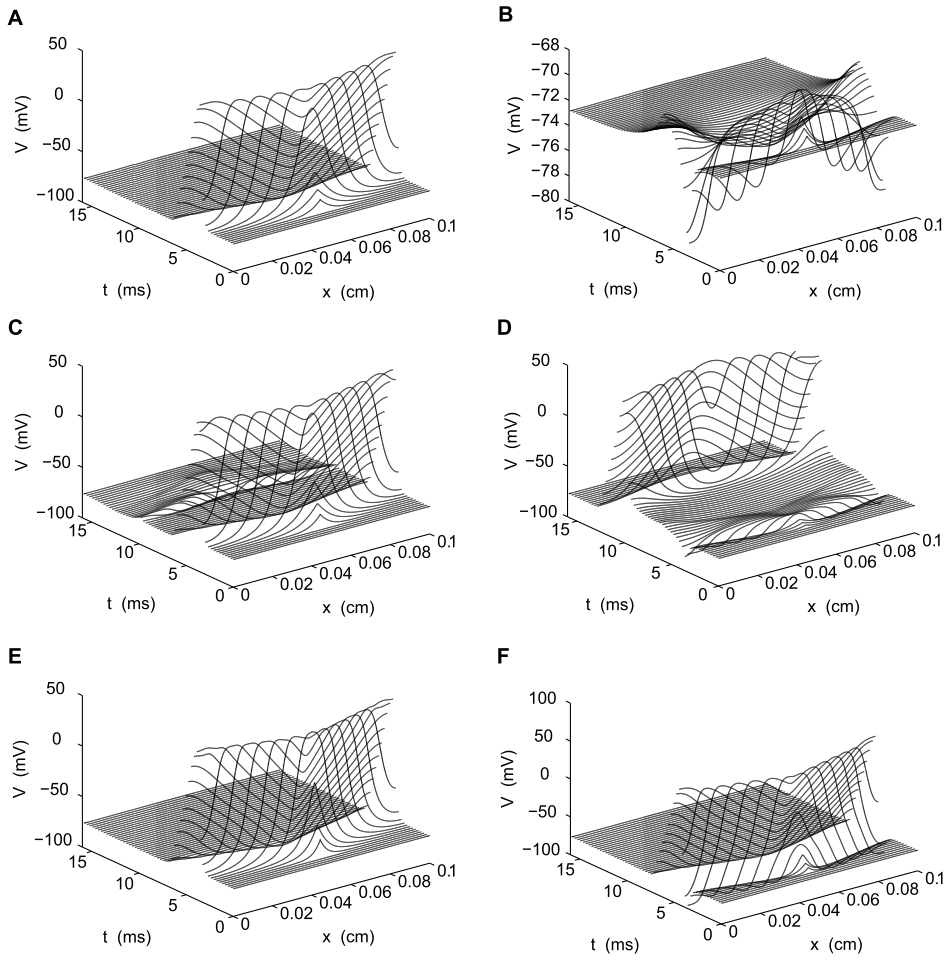

FIGURE 9.6 The full space–time potentials of the two cables (top at left and bottom at right) separated by $2a_0$. Each cable is identical to that examined above in Figure 9.2 and the resistivity of the extracellular medium is $R_e = 0.1$ kΩ cm. We stimulate the top cable with a supra-threshold pulse as in Eq. (9.6) with $I_0 = 400$ pA. This causes an action potential traveling wave in the cable. **A**. With $a_0 = 1.5$ μm the wave in the top cable delivers a complex, but ultimately subthreshold stimulus to the lower cable, as illustrated in **B**. The influence of this upon the top cable appears negligible. **C**. With $a_0 = 1$ μm the wave in the top cable produces a small disturbance in the bottom cable that eventually brings its two ends to threshold. These two end waves travel inward and annihilate each other at the midpoint, see **D**. This latter wave causes a notable, but subthreshold, disturbance in the top cable. **E**. With $a = 0.5$ μm the wave in the top cable quickly ignites a wave in the bottom cable, see **F**. The bottom wave likely lies in the refractory wake of the top wave and therefore provides negligible feedback. (`stE2cab.m`)

9.3 THE ACTIVE NONUNIFORM CABLE

Neurons are not simply nonuniform in their geometry and branching patterns they are also highly nonuniform with regard to their distribution of channels. One simple non-uniformity stems from the observation that many cells partition their "input end" from their "output end" for the obvious reasons that action potentials have a metabolic cost and several inputs ought to arrive in a small window if the subsequent output spike is to mean anything. This partition is often achieved by distributing channels in such a way as to create a weakly excitable dendrite and a strongly excitable cell body. For example, see Figure 9.7, Purkinje and CA3 cells achieve this by decreasing $\overline{g}_{Na}$ with distance from the soma, while CA1 and mitral cells achieve this by increasing $\overline{g}_K$ with distance from the soma.

Before opening the door to wildly branched cells with exotic channel distributions we focus on the straight cable and mimic a weakly excitable dendrite and a highly excitable cell body by assuming that both sodium and potassium peak conductances are constant, except for an excitable "hot spot":

$$\overline{g}_K(x) = 40 - 20\mathbb{1}_{\text{siz}}(x) \quad \text{and} \quad \overline{g}_{Na}(x) = 44 + 560\mathbb{1}_{\text{siz}}(x) \quad \text{where} \quad \text{siz} = (0.005, 0.01) \tag{9.13}$$

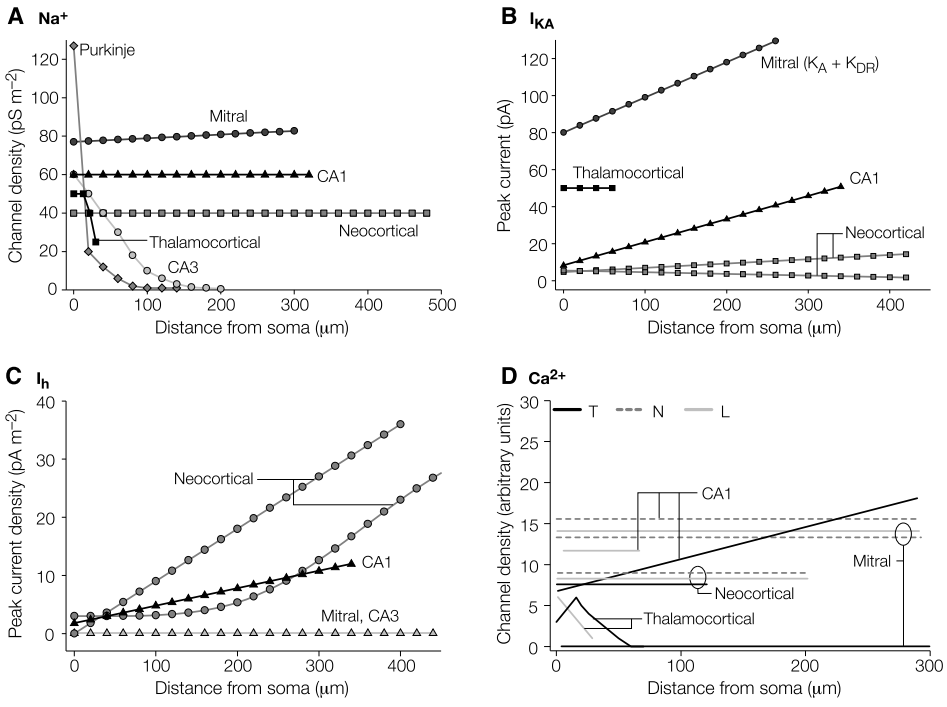

FIGURE 9.7 Channel densities, as a function of distance from the soma, for a variety of cell types and channel types. Here Purkinje denotes the large inhibitory cells of the cerebellum (see Figure 8.1E), the mitral cell is a cell type found in the olfactory bulb, CA1 and CA3 refer to pyramidal cells found in two distinct regions of the hippocampus. **A**. Distribution of sodium channels. In **B**, I_{KA} and K_A refer to the A-type potassium conductance of §4.4, while K_{DR} signifies the delayed rectifier current of §4.1. **C**. Distribution of I_h, the inward rectifier investigated in §5.5. **D**. Distribution of three types of calcium conductances (T, N and L). We will construct models of each of these calcium currents in §14.1. From Migliore and Shepherd (2002).

denotes the spike initiation zone and the cable has length $\ell = 0.1$ cm. We first compute the associated nonuniform rest potential by solving $G_a V_r''(x) = I^{ss}(x)$ where

$$I^{ss}(x, V_r) \equiv \overline{g}_{Na}(x) m_\infty^3(V_r) h_\infty(V_r)(V_r - V_{Na}) + \overline{g}_K(x) n_\infty^4(V_r)(V_r - V_K) + g_{Cl}(V_r - V_{Cl}), \tag{9.14}$$

subject to $V_r'(0) = V_r'(\ell) = 0$. We solve this, as before, via Newton's method with `fsolve` in MATLAB, although here, with perhaps thousands of compartments, this is a much more difficult task. The Jacobian, $\nabla \mathbf{I}^{ss} \in \mathbb{R}^{N_x \times N_x}$,

$$(\nabla \mathbf{I}^{ss})_{ij} = \frac{\partial \mathbf{I}_i^{ss}(\mathbf{V})}{\partial \mathbf{V}_j} \tag{9.15}$$

that springs from the quasi-active counterpart (see §9.4) greatly eases the burden. In particular, writing the discretized rest equation as $G_a \mathbf{S}\mathbf{V} - \mathbf{I}^{ss}(\mathbf{V}) = 0$ we note that Newton's method converges to the (discrete) rest potential via the update rule

$$\mathbf{V}^{k+1} = \mathbf{V}^k - (G_a \mathbf{S} - \nabla \mathbf{I}^{ss}(\mathbf{V}^k)) \backslash (G_a \mathbf{S}\mathbf{V}^k - \mathbf{I}^{ss}(\mathbf{V}^k)).$$

We have coded this in `stEcabnon.m` and illustrate its use in Figure 9.8.

We see in both panels of Figure 9.8 a direct reflection of the cable's nonuniform channel distribution. To better appreciate the impact of Figure 9.8B we show in Figure 9.9 the full spatio-temporal response to a stimulus that is subthreshold when delivered distally but supra-threshold when delivered proximally.

Although the stimulus in Figure 9.9B was delivered to a weak segment of the cable, we see that the entire cable is excitable enough to support a traveling action potential. In addition, as in Figure 9.1, we note that the action potential in the distal region is smaller than that at the siz.

We now focus on the synaptic machinery that detects the presence of such a back-propagating action potential in the postsynaptic cell shortly following presynaptic activity. In particular, we place a spine (recall §6.5) at x_s and

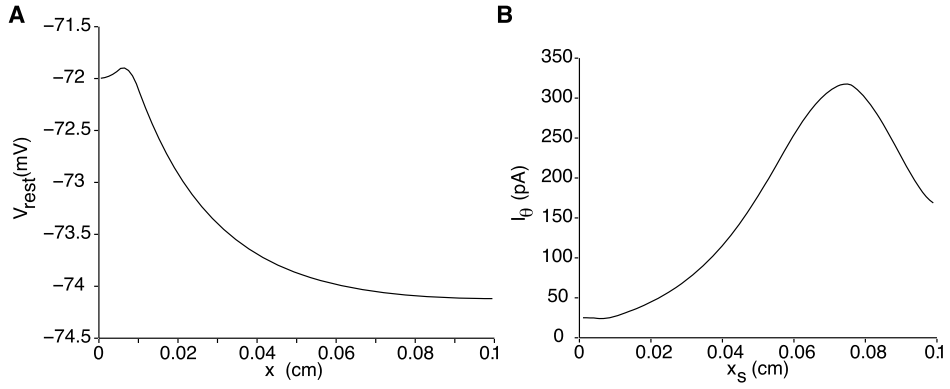

FIGURE 9.8 Rest potential (**A**) and Threshold Current (**B**) for the cable with the nonuniform channel distribution specified in Eq. (9.13). (`stEcabnon.m`)

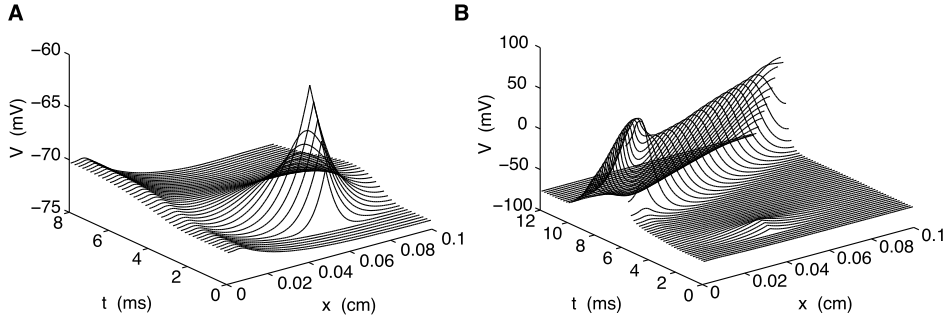

FIGURE 9.9 Response to injection of 200 pA for 1 ms at $x = 0.06$, (**A**), and $x = 0.04$ cm, (**B**). This is not merely a three dimensional view of Figure 9.8B, for here we see that the proximal stimulus did not elicit an action potential at the stimulation site (where the cable is only weakly excitable), but rather was sufficiently strong that it eventually reached the highly excitable zone. (`stEcabnon.m`)

endow its head with two types, AMPA and NMDA, of glutamate receptors. The abbreviation NMDA stands for N-methyl-D-aspartic acid, which is a selective activator (or agonist) of the NMDA receptor (NMDAR), just as AMPA is for the AMPA receptor.

We built a model for AMPA receptors in §2.5. The methodology for NMDARs is similar to a point, for the associated conductance has a strong voltage dependence. If W denotes the spine head transmembrane potential our cable equation takes the form

$$C_m \frac{\partial V}{\partial t} = G_a \frac{\partial^2 V}{\partial x^2} - \overline{g}_{Na} m^3 h (V - V_{Na}) - \overline{g}_K n^4 (V - V_K) - g_{Cl}(V - V_{Cl}) + \gamma_2 (W(t) - V(x,t))\delta(x - x_s)$$

while the spine potential, W, obeys

$$C_m W'(t) + g_{Cl}(W(t) - V_{Cl}) + (g_A(t) + g_N(t) M(W(t)))(W(t) - V_{syn}) = \gamma_1 (V(x_s, t) - W(t)). \tag{9.16}$$

The coupling parameters, as in §6.5, are

$$\gamma_1 = 1/(R_{sn} A_{sh}) \quad \text{and} \quad \gamma_2 = 1/(R_{sn} 2\pi a)$$

while the AMPA and NMDA conductances obey

$$g_A(t) = \overline{g}_A R_A(t) \quad \text{and} \quad g_N(t) = \overline{g}_N R_N(t) \tag{9.17}$$

where R_A and R_N are the respective fractions of activated AMPA and NMDA receptors. We suppose, as in Eq. (2.21), that they obey the first order equations

$$R_A'(t) = k_A^+ \mathcal{T}(t)(1 - R_A(t)) - k_A^- R_A(t) \quad \text{and} \quad R_N'(t) = k_N^+ \mathcal{T}(t)(1 - R_N(t)) - k_N^- R_N(t)$$

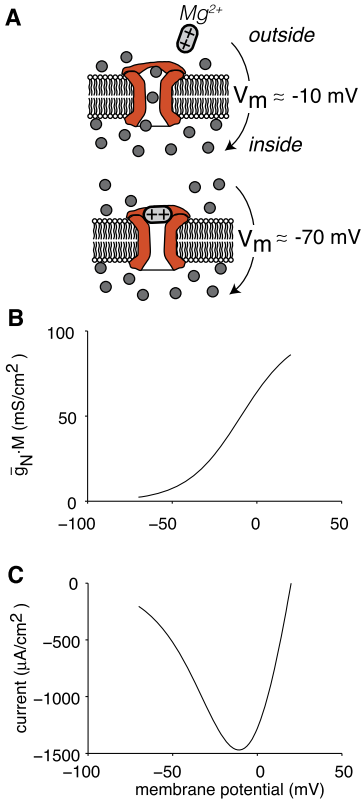

FIGURE 9.10 **A**. Schematic illustration of the block of the NMDA receptor channel by magnesium. At potentials near rest, magnesium enters the pore and blocks the channel (bottom). At depolarized potentials the magnesium is ejected and the channel is free to pass Na^+, K^+ and, most importantly, Ca^{2+}. **B**. Dependence of $\overline{g}_N M$ on W. **C**. Dependence of $\overline{g}_N M(W)(W - V_{syn})$ on W.

where $\mathcal{T}(t)$ is the dosage of glutamate received at the spine head. We encode the voltage dependence of the NMDA receptor in

$$M(W) = \frac{1}{1 + \exp(-aW)[Mg^{2+}]_e/b}, \tag{9.18}$$

where $a = 0.062\ \text{mV}^{-1}$, $b = 3.57$ mM, and $[Mg^{2+}]_e$ (in units of mM) denotes the extracellular concentration of magnesium ions, which is normally equal to 2 mM. These ions block the channel pore associated with the NMDAR from the outside at resting levels of W (Figure 9.10A). This magnesium block is relieved upon sufficient spine depolarization in a manner that is well captured by Eq. (9.18) (Figure 9.10B). As a result, the current flow across the NMDAR channel is a highly non-linear function of W (Figure 9.10C).

Regarding initial conditions, it follows from Eq. (9.16) that the resting spine potential obeys

$$g_{Cl}(W_r - V_{Cl}) = \gamma_1(V_r(x_s) - W_r), \quad \text{that is,} \quad W_r = \frac{g_{Cl}V_{Cl} + \gamma_1 V_r(x_s)}{g_{Cl} + \gamma_1}$$

and so the cable rest potential obeys

$$G_a V_r'' = \overline{g}_{Na} m_\infty^3(V_r) h_\infty(V_r)(V_r - V_{Na}) + \overline{g}_K n_\infty^4(V_r)(V_r - V_K) + g_{Cl}(V_r - V_{Cl}) - \frac{\gamma_2 g_{Cl}}{g_{Cl} + \gamma_1}(V_{Cl} - V_r)\delta(x - x_s).$$

We solve this for V_r precisely as in Eq. (9.15).

If $\mathcal{T}$ is simply a pulse we may invoke the exact solution for R_A and R_N in Eq. (3.35). Let us however proceed more generally and define

$$\mathcal{T}^j = \mathcal{T}((j-1)dt), \quad \text{and} \quad \mathbb{R}_A^j \approx R_A((j-1)dt),$$

and update $\mathtt{R}_A$ via the Backward Euler scheme

$$\mathtt{R}_A^j = \frac{\mathtt{R}_A^{j-1} + dtk_A^+\mathcal{T}^j}{1 + (k_A^+\mathcal{T}^j + k_A^-)dt}.$$

Given the explicit nonlinearity, M in Eq. (9.18), we update $\mathtt{W}$ by the hybrid Backward Euler scheme

$$C_m(\mathtt{W}^j - \mathtt{W}^{j-1})/dt + g_{Cl}(\mathtt{W}^j - V_{Cl}) + (g_A^j + g_N^j M(\mathtt{W}^{j-1}))(\mathtt{W}^j - V_{syn}) = \gamma_1(\mathtt{V}_k^{j-1} - \mathtt{W}^j)$$

or

$$\mathtt{W}^j = \frac{(C_m/dt)\mathtt{W}^{j-1} + g_{Cl}V_{Cl} + (g_A^j + g_N^j M(\mathtt{W}^{j-1}))V_{syn} + \gamma_1\mathtt{V}_k^{j-1}}{(C_m/dt) + g_{Cl} + g_A^j + g_N^j M(\mathtt{W}^{j-1}) + \gamma_1}.$$

We apply the same scheme to the gating variables, e.g.,

$$\mathtt{m}_i^j = \frac{\mathtt{m}_i^{j-1} + dt\alpha_m(\mathtt{V}_i^{j-1})}{1 + dt(\alpha_m(\mathtt{V}_i^{j-1}) + \beta_m(\mathtt{V}_i^{j-1}))},$$

and finally update the cable potential via an honest backward Euler scheme

$$C_m(\mathtt{V}^j - \mathtt{V}^{j-1})/dt = (G_a\mathbf{S} - \mathrm{diag}\,(\mathtt{d}^j))\mathtt{V}^j + \mathtt{f}^j$$

where the elements of $\mathtt{d}^j$ and $\mathtt{f}^j$ are

$$\mathtt{d}_i^j = \overline{g}_{Na}(\mathtt{m}_i^j)^3\mathtt{h}^j + \overline{g}_K(\mathtt{n}_i^j)^4 + g_{Cl} + \gamma_2\delta_{ik} \quad \text{and}$$
$$\mathtt{f}_i^j = \overline{g}_{Na}(\mathtt{m}_i^j)^3\mathtt{h}^j V_{Na} + \overline{g}_K(\mathtt{n}_i^j)^4 V_K + g_{Cl}V_{Cl} + \gamma_2\mathtt{W}^j\delta_{ik}$$

and k is the number of the compartment at which the spine is attached. We now consider a concrete example. We place a spine at $x_s = 0.04$ cm, with the geometric parameters as in Eq. (6.58), and receptor and conductance parameters

$$k_A^+ = 1.1\ (\mathrm{mM\,ms})^{-1}, \quad k_A^- = 0.19\ \mathrm{ms}^{-1}, \quad \text{and} \quad \overline{g}_A = 200\ \mathrm{mS/cm}^2,$$
$$k_N^+ = 0.072\ (\mathrm{mM\,ms})^{-1}, \quad k_N^- = 0.0066\ \mathrm{ms}^{-1}, \quad \text{and} \quad \overline{g}_N = 100\ \mathrm{mS/cm}^2,$$

and synaptic reversal potential $V_{syn} = 20$ mV. On stimulating the spine with a 1 ms pulse of 1 mM glutamate we find, as in Figure 9.9B, slow progression of subthreshold depolarization toward the hot zone followed by a rapid back propagating action potential (BPAP). We plot the salient features in Figure 9.11.

9.4 THE QUASI-ACTIVE CABLE*

If the injected current is small, say εI_{stim}, we may develop V and its gating variables in power series, as in Eq. (5.1), in ε. For example, $V(x,t) = V_r(x) + \varepsilon\tilde{V}(x,t) + O(\varepsilon^2)$, where $V_r(x)$ is the rest potential. As in Eq. (5.2), the linear terms

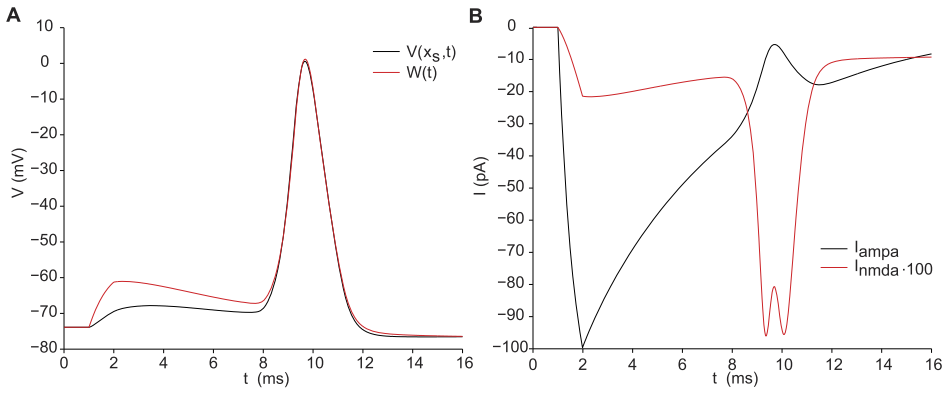

FIGURE 9.11 Potentials (**A**), and currents (**B**), at the spine, on the nonuniform active cable. We see the strong late (from the BPAP) depolarization of the spine head free the magnesium block at the NMDAR and so permit a sizable, inward, NMDA current. This current is the signature of near coincident pre- and postsynaptic activity, and as such forms a natural substrate for the Hebbian learning algorithm of §13.6. To lend it even greater specificity, this current is rich in calcium ions. We will take a careful look at the complex role of Ca^{2+} in spine heads in Chapter 14. (`stEcabspine.m`)

in this expansion obey what we call the quasi-active system

$$\begin{aligned}
\frac{\partial \tilde{m}}{\partial t} &= (\overline{m}'_\infty \tilde{V} - \tilde{m})/\overline{\tau}_m \\
\frac{\partial \tilde{h}}{\partial t} &= (\overline{h}'_\infty \tilde{V} - \tilde{h})/\overline{\tau}_h \\
\frac{\partial \tilde{n}}{\partial t} &= (\overline{n}'_\infty \tilde{V} - \tilde{n})/\overline{\tau}_n \\
C_m \frac{\partial \tilde{V}}{\partial t} &= \lambda^2 \frac{\partial^2 \tilde{V}}{\partial x^2} - \overline{g}_{Na}\{\overline{m}^3 \overline{h} \tilde{V} + (3\tilde{m}\overline{m}^2\overline{h} + \overline{m}^3\tilde{h})v_{Na}\} - \overline{g}_K\{\overline{n}^4\tilde{V} + 4\tilde{n}\overline{n}^3 v_K\} \\
&\quad - g_{Cl}\tilde{V} + I_{stim}(x,t)/(2\pi a),
\end{aligned} \tag{9.19}$$

where $\overline{m}(x) \equiv m_\infty(V_r(x))$, $\overline{\tau}_m \equiv \tau_m(V_r(x))$ and $\overline{m}'_\infty \equiv m'_\infty(V_r(x))$. We gather the unknowns in $\mathbf{y} \equiv (\tilde{m}\ \tilde{h}\ \tilde{n}\ \tilde{V})^T$ and represent Eq. (9.19) as

$$\frac{\partial \mathbf{y}}{\partial t} = \mathbf{B}\mathbf{y} + \mathbf{f} \tag{9.20}$$

where $\mathbf{f} = I_{stim}(x,t)/(2\pi a C_m)(0\ 0\ 0\ 1)^T$ and $\mathbf{B}$ is the matrix differential operator

$$\mathbf{B} = \begin{pmatrix} -1/\overline{\tau}_m & 0 & 0 & \overline{m}'_\infty/\overline{\tau}_m \\ 0 & -1/\overline{\tau}_h & 0 & \overline{h}'_\infty/\overline{\tau}_h \\ 0 & 0 & -1/\overline{\tau}_n & \overline{n}'_\infty/\overline{\tau}_n \\ -3\overline{m}^2\overline{h}v_{Na}/\tau_{Na} & -\overline{m}^3 v_{Na}/\tau_{Na} & -4\overline{n}^3 v_K/\tau_K & (\lambda^2/\tau)\partial_{xx} - \gamma \end{pmatrix} \tag{9.21}$$

where $\gamma = \overline{m}^3\overline{h}/\tau_{Na} + \overline{n}^4/\tau_K + 1/\tau_{Cl}$. We have discretized (precisely as in the past three sections) and coded this system in `stEQcab.m`. We contrast the quasi-active and active responses of the uniform cable to random current stimuli in `stEcabQandA.m` and illustrate our findings in Figure 9.12.

Figure 9.12 indicates that the quasi-active model is an accurate predictor of the cumulative response to subthreshold spatio-temporal input. We next investigate its ability to predict the cell's resonant frequency.

Resonance. We expect the resonant frequencies of the active cable to be reflected in the imaginary parts of the eigenvalues of $\mathbf{B}$. As in §5.3 we write

$$\mathbf{B}\mathbf{w}(x) = \zeta \mathbf{w}(x) \quad \text{with} \quad \mathbf{w} \equiv (\mu(x)\ \eta(x)\ \nu(x)\ q(x))^T$$

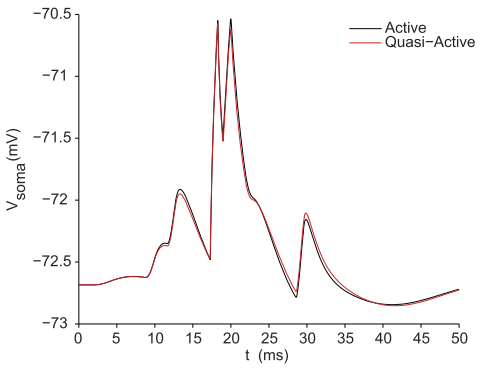

FIGURE 9.12 The voltage response at $x = 0$, for both the active and quasi-active uniform cable, to 10 current stimuli, each 1 ms in duration and 20 pA in amplitude, with random start times and locations. Compare with Figure 5.1. (`stEcabQandA.m`)

and deduce that

$$\overline{m}'_\infty q - \mu = \zeta \overline{\tau}_m \mu \quad \text{so} \quad \mu = \frac{\overline{m}'_\infty}{1 + \zeta \overline{\tau}_m} q.$$

The other gating variables follow suit, namely

$$\eta = \frac{\overline{h}'_\infty}{1 + \zeta \overline{\tau}_h} q \quad \text{and} \quad \nu = \frac{\overline{n}'_\infty}{1 + \zeta \overline{\tau}_n} q$$

and so the equation for the quasi-potential, q, reads

$$(\lambda^2/\tau) q'' - \left(\gamma + \frac{3\overline{m}^2 \overline{h} v_{Na} \overline{m}'_\infty}{\tau_{Na}(1 + \zeta \overline{\tau}_m)} + \frac{\overline{m}^3 v_{Na} \overline{h}'_\infty}{\tau_{Na}(1 + \zeta \overline{\tau}_h)} + \frac{4\overline{n}^3 v_K \overline{n}'_\infty}{\tau_K (1 + \zeta \overline{\tau}_n)} \right) q = \zeta q. \tag{9.22}$$

If the cable is uniform then the large bracketed term is independent of x and we may choose q to be the nth eigenfunction, Eq. (6.39), of the passive uniform cable. As $q_n'' = \vartheta_n q_n$ Eq. (9.22) becomes

$$(\lambda^2/\tau) \vartheta_n q_n - \left(\gamma + \frac{3\overline{m}^2 \overline{h} v_{Na} \overline{m}'_\infty}{\tau_{Na}(1 + \zeta \overline{\tau}_m)} + \frac{\overline{m}^3 v_{Na} \overline{h}'_\infty}{\tau_{Na}(1 + \zeta \overline{\tau}_h)} + \frac{4\overline{n}^3 v_K \overline{n}'_\infty}{\tau_K (1 + \zeta \overline{\tau}_n)} \right) q_n = \zeta q_n.$$

On canceling the common q_n we find that the eigenvalue, ζ, must be a root of the quartic

$$\begin{aligned} P_n(\zeta) = {} & (\zeta + \gamma - (\lambda^2/\tau)\vartheta_n)(1 + \zeta \overline{\tau}_m)(1 + \zeta \overline{\tau}_h)(1 + \zeta \overline{\tau}_n) + 3\overline{m}^2 \overline{h} v_{Na} \overline{m}'_\infty (1 + \zeta \overline{\tau}_h)(1 + \zeta \overline{\tau}_n)/\tau_{Na} \\ & + \overline{m}^3 v_{Na} \overline{h}'_\infty (1 + \zeta \overline{\tau}_m)(1 + \zeta \overline{\tau}_n)/\tau_{Na} + 4\overline{n}^3 v_K \overline{n}'_\infty (1 + \zeta \overline{\tau}_m)(1 + \zeta \overline{\tau}_h)/\tau_K. \end{aligned} \tag{9.23}$$

We label these roots

$$\zeta_{n,j}, \quad n = 0, 1, 2, \ldots, \quad j = 1, 2, 3, 4$$

and illustrate them in Figure 9.13 for uniform cables of differing lengths. As $\vartheta_0 = 0$ it follows that the roots of P_0 are precisely those of the space-clamped isopotential cable (recall Eq. (5.24)).

As in §5.3, the associated eigenfunctions of $\mathbf{B}$ for the uniform cable are

$$\mathbf{w}_{n,j}(x) = \left(\frac{\overline{m}'_\infty}{1 + \zeta_{n,j} \overline{\tau}_m} q_n(x) \quad \frac{\overline{h}'_\infty}{1 + \zeta_{n,j} \overline{\tau}_h} q_n(x) \quad \frac{\overline{n}'_\infty}{1 + \zeta_{n,j} \overline{\tau}_n} q_n(x) \quad q_n(x) \right)^T \tag{9.24}$$

and so if

$$I_{stim}(x,t) = \sum_{n=0}^{\infty} I_{stim,n}(t) q_n(x), \quad \text{i.e.,} \quad I_{stim,n}(t) = \int_0^\ell I_{stim}(x,t) q_n(x)\, dx,$$

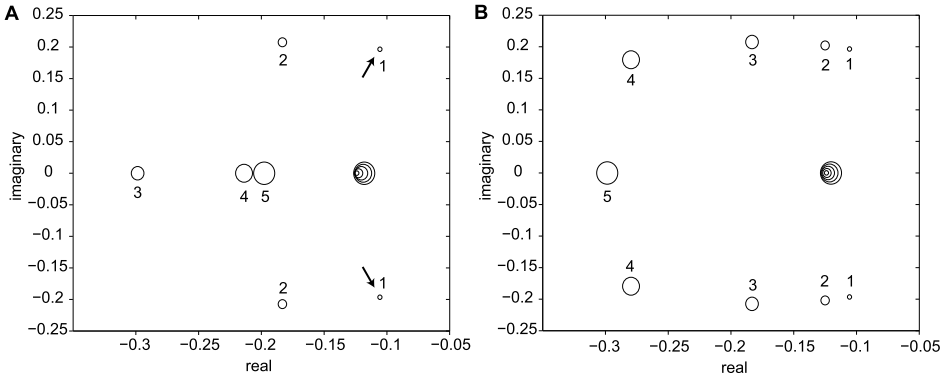

FIGURE 9.13 The roots of the quartic P_n, Eq. (9.23), for $n = 0, 1, 2, 3, 4, 5$. The radius of the enclosing circle doubles with n. **A**. $\ell = 1$ mm. **B**. $\ell = 2$ mm. Regarding resonance our interest is in nonreal eigenvalues with large real part (arrows on plot). We observe that these occur for $n = 0$ and so correspond to the constant eigenvector, q_0. We also observe that although the longer cable possesses more nonreal eigenvalues, the nonreal eigenvalue with the largest real part is the same in the two cases. Note that the cable length, ℓ, enters P_n via $\vartheta_n = -(n\pi/\ell)^2$ and so is not seen by P_0. (`quasicabspec.m`)

then the full stimulus vector enjoys the expansion

$$\mathbf{f} = \sum_{n=0}^{\infty} \sum_{j=1}^{4} c_{n,j}(t)\mathbf{w}_{n,j}(x)$$

where, recalling Eq. (5.26),

$$c_{n,j}(t) = \frac{I_{stim,n}(t)}{2\pi a C_m} \frac{(1+\zeta_{n,j}\overline{\tau}_m)(1+\zeta_{n,j}\overline{\tau}_h)(1+\zeta_{n,j}\overline{\tau}_n)}{\overline{\tau}_m\overline{\tau}_h\overline{\tau}_n \prod_{k\neq j}(\zeta_{n,j}-\zeta_{n,k})}. \tag{9.25}$$

It follows that

$$\boxed{\tilde{V}(x,t) = \sum_{n=0}^{\infty} q_n(x) \sum_{j=0}^{3} \int_0^t c_{n,j}(s)\exp((s-t)\zeta_{n,j})ds} \tag{9.26}$$

is the response, with respect to rest, of the quasi-active uniform cable.

We next investigate, in Figure 9.14, the impact of nonuniform channel distribution on the eigenvalues and eigenvectors of the quasi-active system. In this case, although the eigenvectors retain the functional form in Eq. (9.24), the nonuniformity of the coefficients in Eq. (9.22) prohibit its exact solution. We therefore turn to numerical means. We have coded the discretized nonuniform eigenvalue problem in `Qcabnon.m`.

We now investigate the correspondence between the spectra of the uniform and nonuniform quasi-active cables and the associated resonance, or input resistance, curves of the corresponding active cables. In particular, we drive the uniform and nonuniform active cables with the distributed current

$$I_{stim}(x,t) = I_0 \sin(2\pi\omega t)\,\mathrm{Re}(q_0(x)) \tag{9.27}$$

where $\mathrm{Re}(q_0)$ is the real part of the eigenvector of **B** associated with the nonreal eigenvalue of greatest real part for the uniform, and nonuniform quasi-active cables, respectively. These two spatial distributions of current will maximize the respective resonances. We drive the cable until time T, where T is large enough to get past the initial transient, then compute

$$V_{max,\infty} \equiv \max_{\substack{0\le x\le \ell \\ t>T/2}} V(x,t) \tag{9.28}$$

and examine, in Figure 9.15 the dependence of the associated input resistance on input frequency.

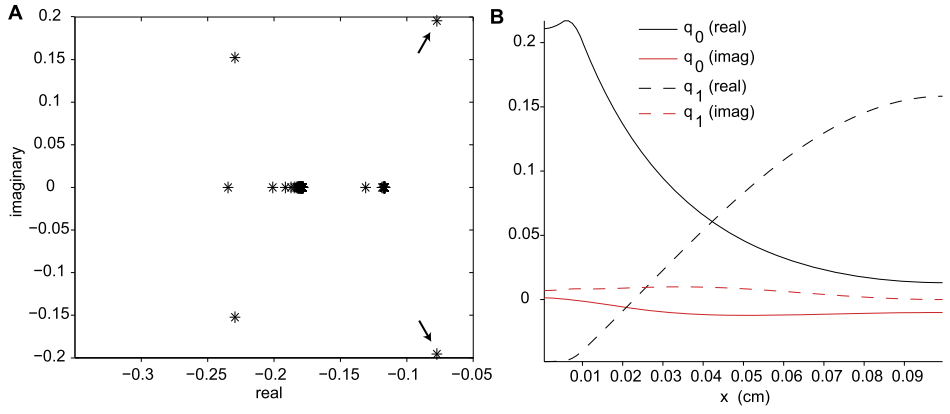

FIGURE 9.14 Eigenvalues (**A**), and Eigenvectors (**B**), of the quasi-active operator **B** when the active conductances are distributed per Eq. (9.13). Regarding panel **A**: since the nonreal eigenvalue with the greatest real part has moved right in comparison to Figure 9.13 (see arrows on plot), we expect the associated input resistance to have a sharper peak. The eigenvectors in **B**, labeled q_0 and q_1, correspond to the two pair of nonreal eigenvalues in **A**, with q_0 associated with the nonreal eigenvalue of greatest real part. Compare to Figure 6.2. (`Qcabnon.m`)

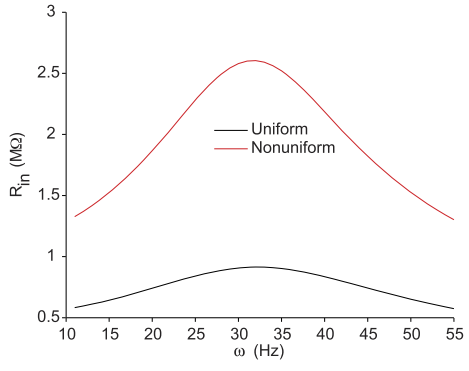

FIGURE 9.15 Input resistance, $R_{in}(\omega) = V_{max,\infty}/I_0$, of the active cable where $I_0 = 10$ pA and ω are prescribed in Eq. (9.27) and $V_{max,\infty}$ in Eq. (9.28). As predicted by the two quasi-active spectra, the nonuniformity has yielded a sharper resonant peak. (`stEcabResdrive.m`)

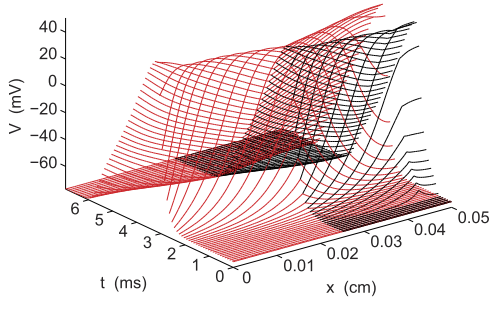

FIGURE 9.16 Action potential propagation in the active uniform fork. A 1 ms supra-threshold current pulse was delivered near the distal end of the black daughter at 0.5 ms. We see her depolarize and initiate a wave that travels in both directions. As it reaches the branch point the wave splits and travels down the mother and up the other daughter. (`stEfork.m`)

9.5 THE ACTIVE DENDRITIC TREE

We return to the forked cell with geometric and passive parameters as in Eq. (8.7) and Eq. (8.8). To this we add the standard Hodgkin–Huxley channels and investigate action potential wave propagation (Figure 9.16), threshold, attenuation and synaptic integration (Figure 9.17 and Figure 9.18).

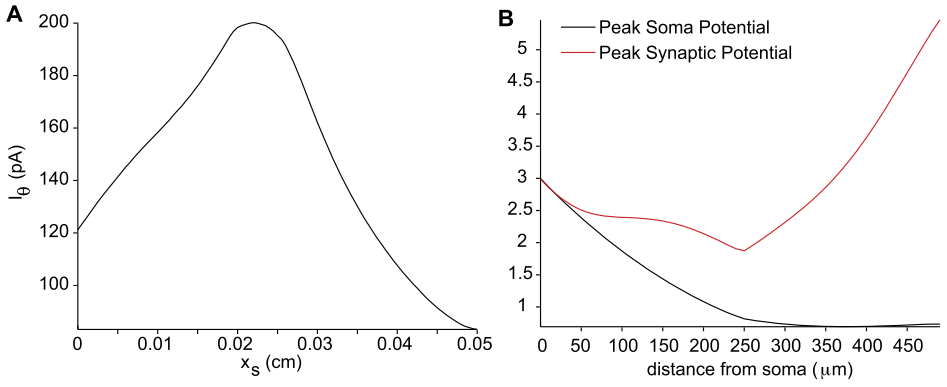

FIGURE 9.17 The active uniform fork. **A**. Threshold at which a 1 ms current pulse will generate an action potential, as a function of stimulation site. **B**. Peak somatic and synaptic potentials (in units of mV). (`stEforksyngain.m`)

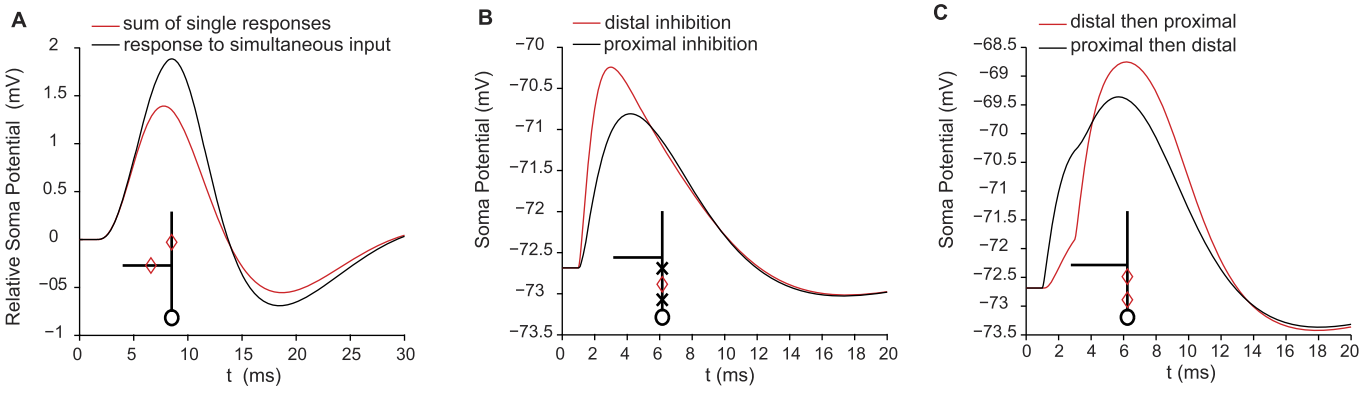

FIGURE 9.18 The response at the cell body of the active uniform fork to a pair of synaptic inputs. **A**. Comparison of response to simultaneous dual excitation (red) to the sum of the responses to individual excitations (black). In these two cases we report the relative soma potential, $V(\ell_3, t) - V_r(\ell_3)$. **B**. Comparison of response of distal (red) and proximal (black) inhibition of a fixed excitatory input. **C**. Comparison of distal before proximal excitatory input to proximal before distal excitatory input. (`stEforksyndrive.m`)

The minimum current required to elicit such a wave is revealed in Figure 9.17A. We next repeat the experiment of Figure 8.7. That is, we compute the maximal somatic and synaptic potentials arising from a single alpha-synaptic input, as the synapse is placed at successively more distal locations. We illustrate our findings in Figure 9.17B.

We next investigate the active tree's integration of two synaptic inputs. For simplicity we will illustrate our findings for the uniform active tree. In each case, each synapse will be described by an alpha function with $\overline{g}_{syn} = 0.5$ nS and $\tau_\alpha = 1$ ms, though typically inhibitory GABA synapses have longer time constants (≈ 5 ms) than excitatory AMPA synapses. For excitatory synapses we use $V_{syn} = 0$ and for inhibitory $V_{syn} = -70$ mV.

In our first simulation we contrast the response at the soma to simultaneous excitatory input into the two daughters with the sum of the responses to individual input. The placement of the synapses is illustrated in the inset to Figure 9.18A. The corresponding curves demonstrate the cell's strong nonlinear amplification of the two inputs.

In our second simulation we contrast distal and proximal inhibition of a fixed excitatory input. The placement is illustrated in the inset to Figure 9.18B. The red diamond marks the excitatory synapse while the inhibitory synapse is placed at either, but not both, the proximal or distal black x. The corresponding curves demonstrate that proximal inhibition offers significantly more attenuation.

In our two previous examples our two synapses were presumed to fire simultaneously. For our third simulation we contrast the timing of distal and proximal excitatory input. The placement of the synapses is illustrated in the inset to Figure 9.18C. The two inputs were separated in time by 2 ms. The corresponding curves demonstrate that distal before proximal offers a greater boost than proximal before distal.

Upon the active fork we have been able to illustrate the basic notions of action potential propagation and synaptic integration. Most cells, recall Figure 8.1, however possess tens and often hundreds of tapered branches. The modeling

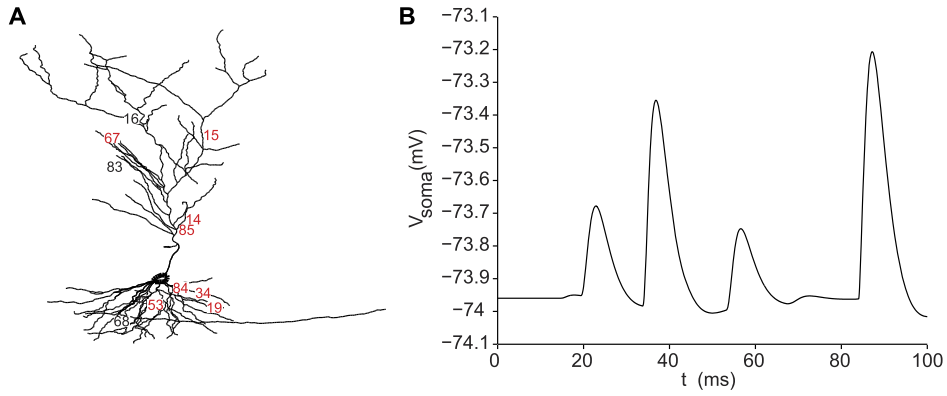

FIGURE 9.19 The response at the cell body to 12 synaptic inputs. The cell model is weakly excitable, $\overline{g}_K = 40$, $\overline{g}_{Na} = 40$ mS/cm^2, with a highly excitable cell body $\overline{g}_K = 20$ and $\overline{g}_{Na} = 600$ mS/cm^2. **A**. Alpha synapses, $\overline{g}_{syn} = 0.75$ nS and $\tau_\alpha = 1$ ms, are placed at the locations shown. Red for excitatory, $V_{syn} = 0$, and black for inhibitory, $V_{syn} = -70$ mV. The number indicates the activation time. **B**. The resulting response at the cell body. (`stEtreesyn.m`)

of such structures proceeds as above, i.e., we compartmentalize, balance currents, and construct the associated Hines matrix. The compartmentalization is however preceded by a manual or automatic "tracing" of the cell's morphology. There are now two standard formats, `asc` and `swc`, for files that represent these tracings, see Cannon et al. (1998). We have included converters for both types, `ascconverter.m` and `swcconverter.m`, as well as routines that make the common morphology data structure and Hines matrix, `makemd.m` and `makeH.m`, and finally a routine for viewing the tree, `treeplot.m`. With these we may extend `stEforksyn.m` to `stEtreesyn.m` and so permit the MATLAB simulation of practically all traced cells. For example, we examine in Figure 9.19 a pyramidal cell from the CA1 region of the rodent hippocampus.

9.6 SUMMARY AND SOURCES

We have constructed a mathematical model of a uniform active cable and combined our computational approaches to the active isopotential cell and passive cable to produce an efficient mean for investigating (a) the threshold at which current injection ignites a traveling action potential and (b) the impact of this traveling wave upon neighboring cables. As in the isopotential case the quasi-active approximation performs well in the subthreshold regime. We examine this system more closely in §16.4. We extended our model to active, branched, nonuniform, spiny cables and demonstrated how distal subthreshold synaptic input may be transferred by the cable to a region where it suffices to ignite an action potential that travels both down the cell's axon and up into its dendritic tree. As the action potential reaches the spine(s) that spawned its ignition it opens synaptic NMDA channels that permit calcium into those spines whose presynaptic activity lead the cell to fire. We will see that spinal calcium may in turn result in synaptic plasticity.

The active cable equation was posed and studied by Hodgkin and Huxley (1952). Through a mix of analytical and computational methods they demonstrated that the equation was consistent with action potentials that traveled at speeds very close to those observed in the giant axon of the squid. The section on ephaptic interaction of two cables was suggested by Scott (2002). For further background see Jefferys (1995). The kinetic schemes and parameters of the AMPA and NMDA receptors in §9.3 are drawn from Destexhe et al. (1998). Although we have adopted MATLAB as a platform for modeling, simulation and analysis, there are excellent software tools that are tailored for both modeling and simulation of single neurons as well as circuits. The two most commonly used are GENESIS, see Bower and Beeman (1998), and NEURON, see Carnevale and Hines (2006). We examine the impact of myelin on axonal wave propagation in Exercises 3–5. FitzHugh (1962) is one of the first models of the myelinated axon. For a recent historical review of myelin, see Hartline and Colman (2007). Exercise 6 considers large scale synaptic input into a finely branched cell in a manner motivated by Destexhe et al. (2001).

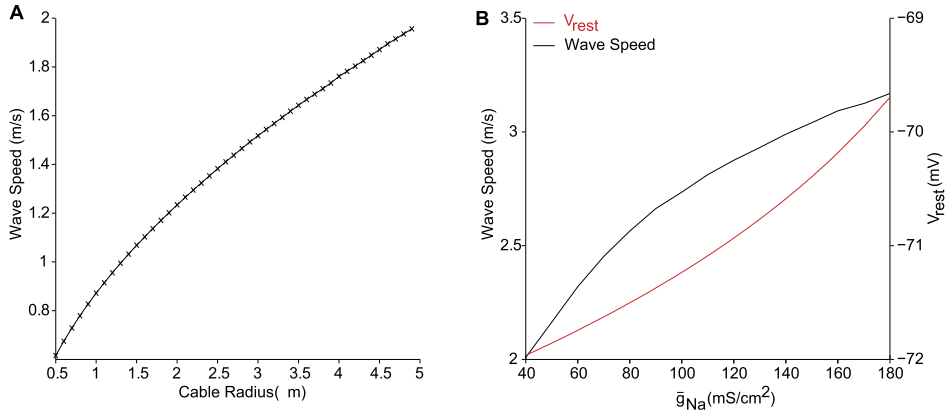

FIGURE 9.20 **A**. Traveling action potential wave speed of the active uniform cable of Figure 9.2 as a function of cable radius. **B**. Rest potential and action potential wave speed of the active uniform cable of Figure 9.2 as a function of maximal sodium conductance, $\overline{g}_{Na}$. (`stEcabsdriver.m` and `stEcabgNadriver.m`)

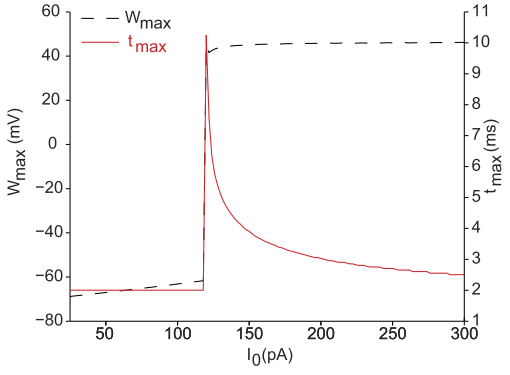

FIGURE 9.21 The maximum midcable depolarization, and the time at which it occurs, in an active uniform cable of radius 1 µm that is 2 µm away from a second cable of radius 1 µm. This second cable receives a midcable, 1 ms, 400 pA current stimulus, while the first cable receives a midcable, 1 ms current injection of amplitude I_0. On comparing with Figure 9.2B we find that the active neighbor lowers the threshold from 150 to 120 pA. (`stE2cabthresh.m`)

9.7 EXERCISES

1. Investigate the impact of cable radius and $\overline{g}_{Na}$ on the velocity of the action potential that propagates down the active uniform cable. In particular, modify `stEcab.m` to produce Figure 9.20.
2. †Investigate the extent to which an excited cable lowers the threshold of its neighbors. In particular, modify `stE2cab.m` to produce Figure 9.21.
3. We have seen that wave speed along cables can be increased by increasing either the cable radius or the density of sodium channels. As each of these comes with high metabolic costs a third way, based on insulation, has evolved. Many long axons in the nervous system of vertebrates (and invertebrates as well) are wrapped with layers of fat, known as myelin.
   These layers are outgrowths of neighboring glial cells. As myelin is only a passive conductor, in order for the wrapped axon to support a traveling action potential the myelin is periodically perforated, exposing the underlying cable at what are known as Nodes of Ranvier, see Figure 9.22A. The distribution of Na^+ and K^+ channels at nodes of Ranvier is highly specific, as illustrated in Figure 9.22B. We will build and investigate, in a series of exercises, a simple model of a myelinated cable. In particular, we will assume that the roughly 100 layers of myelin serve to decrease both the membrane capacitance and conductance by a factor of 100 and that the cable expresses active conductances only at the nodes of Ranvier. Modify `stEcab.m` to accept two new parameters, `id`, the internodal distance, and `nnor`, the number of nodes of Ranvier and so reproduce Figure 9.23.

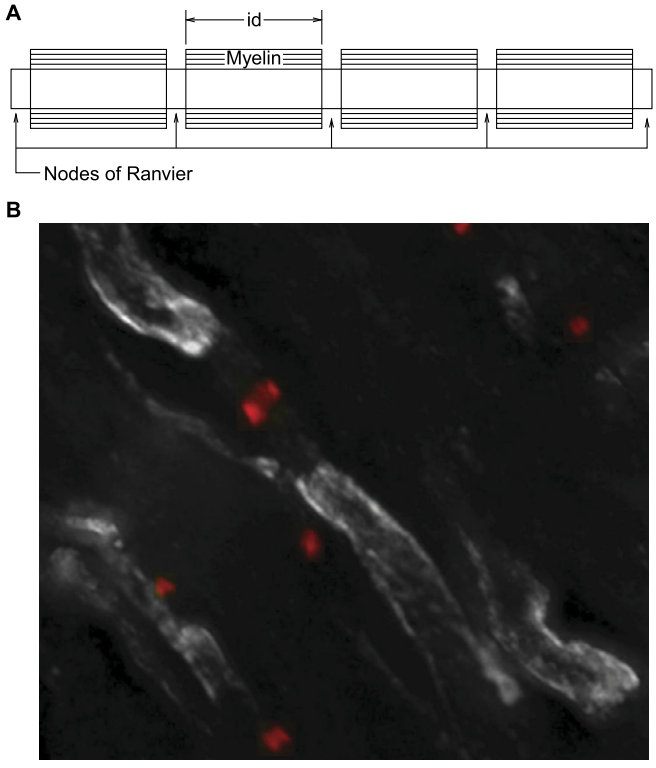

FIGURE 9.22 **A**. Schematic cross-section of a segment of myelinated cable. **B**. Double-labeled micrograph of myelinated axons in the optic nerve illustrating the distribution of channels at nodes of Ranvier. The staining is for Na^+ channels in red, and Kv1.2 K^+ channels in gray. The Na^+ channels are localized at the nodes which typically measure 1 µm in length along the nerve fiber. The K^+ channels are localized in the paranodal region. Micrograph courtesy of Dr. M.N. Rasband, Dept. of Neuroscience, Baylor College of Medicine, Houston, TX.

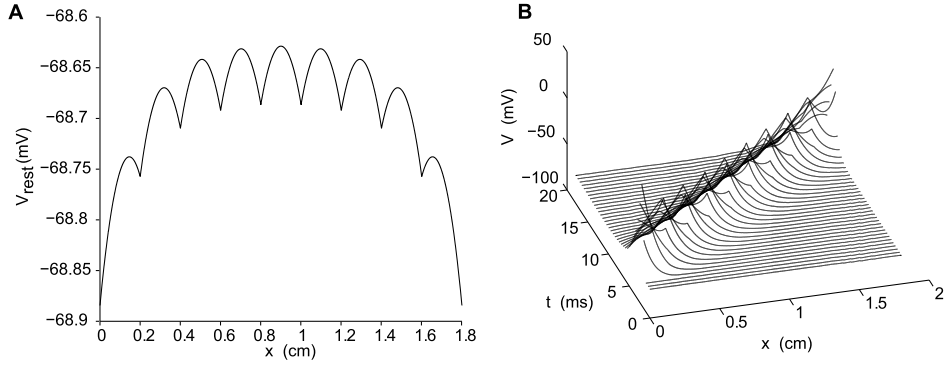

FIGURE 9.23 The rest potential, (**A**), and traveling action potential, (**B**), in a myelinated cable of radius 1 µm with 10 nodes, an internodal distance $id = 2$ mm, a node length of 2 µm, and a step size $dx = 1$ µm. Two of the ten nodes appear at the cable's two ends. The cable was driven with a 1 ms, 50 pA current pulse at the first node. The membrane capacitance was 1 µF/cm^2 in each nodal compartment and 0.01 in each internodal compartment. The membrane conductance was 0.3 mS/cm^2 in each nodal compartment and 0.003 in each internodal compartment. The sodium conductance density was 120 mS/cm^2 in each nodal compartment and 0 in each internodal compartment. The potassium conductance density was 36 mS/cm^2 in each nodal compartment and 0 in each internodal compartment. (`myelins.m`)

4. †We note in Figure 9.23B that the potential dips between nodes. Please modify your code from the previous exercise in order to ascertain, as in Figure 9.24, the dependence of action potential wave speed on internodal distance and cable radius.

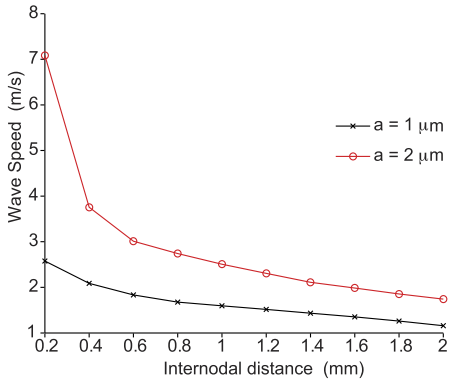

FIGURE 9.24 Action potential wave speed of the myelinated cable. The wave slows as the internodal distance grows. (`myelinsdriver.m`)

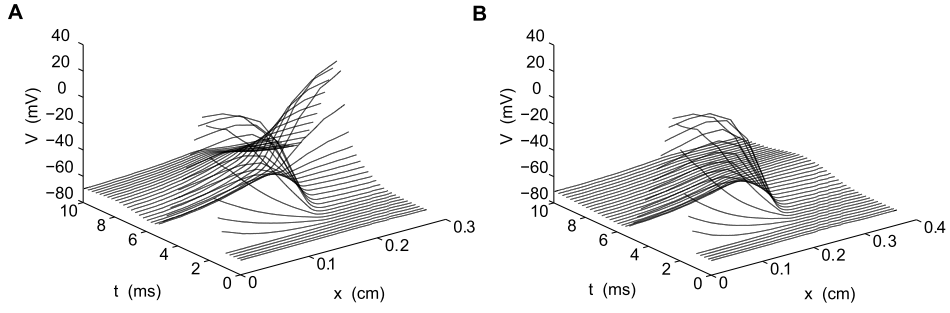

FIGURE 9.25 Conduction block in a partial demyelinated cable. This is the cable used in Figure 9.23 except that $C_m = 1\ \mu\text{F/cm}^2$ and $g_{Cl} = 0.3\ \text{mS/cm}^2$ in the sixth internodal segment. **A**. With an internodal distance $id = 300\ \mu\text{m}$ we see conduction slow in the demyelinated segment and then recover. **B**. With an internodal distance of $id = 400\ \mu\text{m}$ the wave stagnates in the demyelinated segment. (`demyelin.m`)

5. Diseases such as multiple sclerosis are characterized by the systematic, and typically irreversible, loss of myelin. To understand how this can lead to loss of function please modify your code from Exercise 3 to reflect the loss of the sixth segment of myelin and so reproduce the findings of Figure 9.25.
6. We now consider the impact of large scale synaptic input onto a realistic cell. The cell's `asc` file is called `sep12a.asc` and has been plotted using `treeplot.m` in Figure 9.26A. Please modify `stEtreesyn.m` to reproduce the remaining panels in Figure 9.26 and Figure 9.27.
   With a compartment size of 2 μm the cell is subdivided in 945 compartments. We assume the branches to be weakly excitable, $\overline{g}_K = \overline{g}_{Na} = 40\ \text{mS/cm}^2$, and the cell body to be strongly excitable, $\overline{g}_K = 20$ and $\overline{g}_{Na} = 600\ \text{mS/cm}^2$. The leakage conductance is everywhere $1/15\ \text{mS/cm}^2$. We place an α-synapse at every compartment. Eighty percent are presumed excitatory, $V_e = 0\ \text{mV}$ and $\tau_e = 0.5\ \text{ms}$, and the remainder are inhibitory, $V_i = -80\ \text{mV}$ and $\tau_i = 1\ \text{ms}$. Their locations and start times are randomly chosen from the uniform distribution. The maximal excitatory conductance, $\overline{g}_e$, is normally distributed with mean 1 nS and variance 0.01 nS, while the maximal inhibitory conductance, $\overline{g}_i$, is normally distributed with mean 2 nS and variance 0.01 nS. We illustrate the cell and the mean conductance waveforms and their activation in space and time in Figure 9.26.
   In order to discern the "effective" synaptic impact we clamp the soma, as in Exercise 8.4, at $V_{c,1}$ and record the ensuing clamp current, $I_{c,1}(t)$, and then repeat this at a second clamp potential, $V_{c,2}$, and record the ensuing clamp current, $I_{c,2}(t)$. These currents are plotted in Figure 9.27A. With this data we may reverse engineer the effective conductances by solving

$$\begin{aligned} g_e(t)(V_{c,1} - V_e) + g_i(t)(V_{c,1} - V_i) &= I_{c,1}(t) \\ g_e(t)(V_{c,2} - V_e) + g_i(t)(V_{c,2} - V_i) &= I_{c,2}(t) \end{aligned} \tag{9.29}$$

   for g_e and g_i. The results are presented in Figure 9.27B, C and D.
   As a preview of §19.4 we also record the associated power spectra in Figure 9.28.

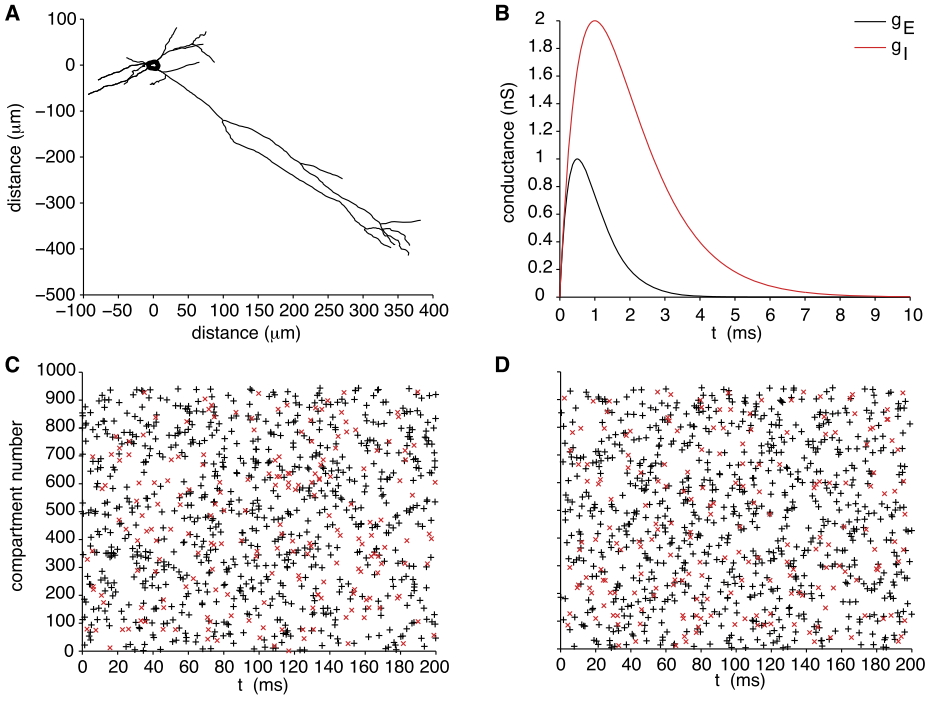

FIGURE 9.26 **A**. Pyramidal cell from the rat entorhinal cortex. **B**. Unitary excitatory and inhibitory conductance time-courses. **C** and **D**. Two instances of random synaptic input into the cell of **A**. Each black + corresponds to an excitatory input, g_e as in **B**, at the associated compartment at the designated time. Each red x corresponds to an inhibitory input, g_i as in **B**, at the associated compartment at the designated time. (`drfsenoper.m`)

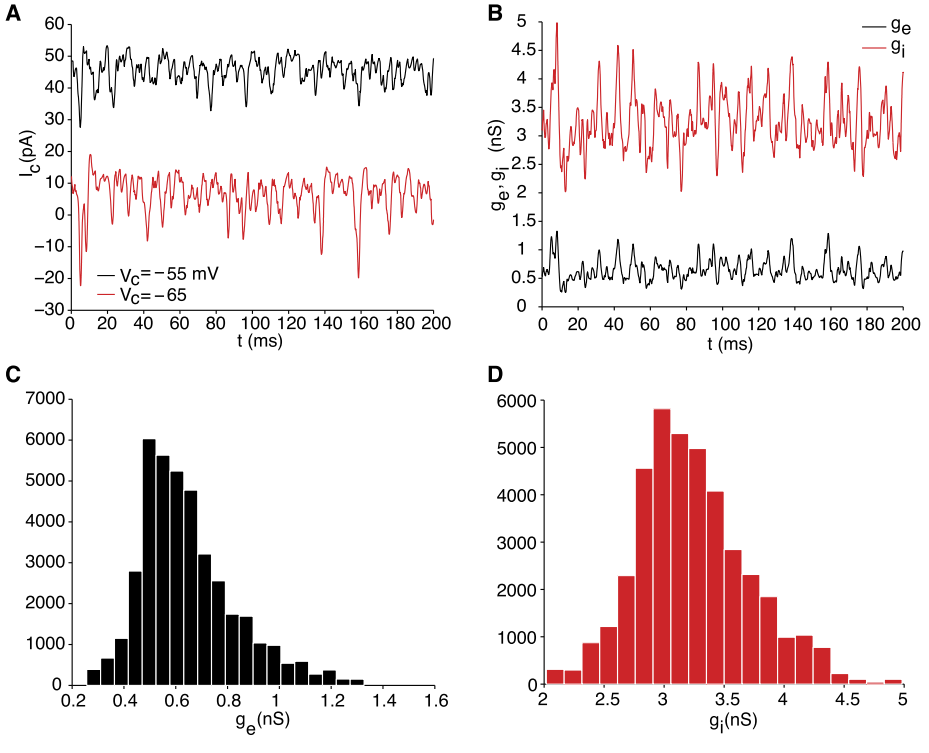

FIGURE 9.27 **A**. The current required to clamp the soma at $V = V_c$ throughout synaptic bombardment. When clamped at −65 mV we used the synaptic schedule of Figure 9.26**C** while when clamping at −55 mV we used the synaptic schedule of Figure 9.26**D**. **B**. Effective excitatory and inhibitory conductances derived from **A** and Eq. (9.29). **C** and **D**. Histograms of the solution to Eq. (9.29) associated with the data in **A**. (`drfsenoper.m`)

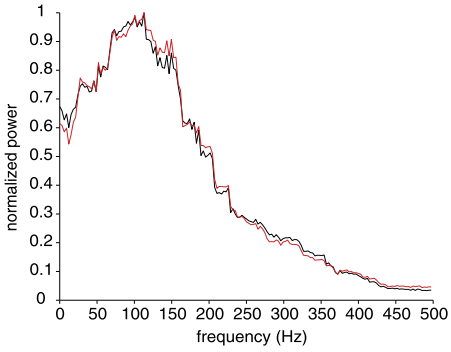

FIGURE 9.28 Power spectra of the excitatory and inhibitory conductances plotted in black and red, respectively. The peak value has been normalized to one. (`drfsenoper.m`)

7. †Modify `stEcab` to compute

$$[Na^+]_{i,AP} = \frac{-2\pi a}{\pi a^2 \ell F} \int_0^T \int_0^\ell I_{Na}(x,t)\, dx\, dt \quad \text{mM}, \tag{9.30}$$

the change, per action potential, in intracellular concentration of Na^+ in an active uniform cable of length ℓ and radius a. Here $F = 96485$ C/mol is Faraday's constant. Using the model parameters that generated the action potential in Figure 9.2A, including $T = 0.008$ s, should yield $[Na^+]_{i,AP} \approx 0.376$ mM. How does this answer compare to the isopotential calculation made in (4.22)? How do their cell volumes compare?